



Surface decorated cobalt sulfide as efficient catalyst for oxygen evolution reaction and its intrinsic activity



Jingde Li^{a,b,1}, Guihua Liu^{b,1}, Jing Fu^b, Gaopeng Jiang^b, Dan Luo^b, Fathy M. Hassan^b, Jing Zhang^b, Ya-Ping Deng^b, Pan Xu^b, Luis Ricardez-Sandoval^b, Zhongwei Chen^{b,*}

^a School of Chemical Engineering and Technology, Hebei University of Technology, Tianjin, 300130, China

^b Department of Chemical Engineering, University of Waterloo, Waterloo, ON N2L 3G1, Canada

ARTICLE INFO

Article history:

Received 24 May 2018

Revised 27 July 2018

Accepted 22 August 2018

Keywords:

Density functional calculations

Oxygen evolution reaction

Cobalt sulfide

Metal chalcogenides

Zinc-air battery

ABSTRACT

Here, we report an efficient surface decorated, e.g. oxidation and nitrogen doped, cobalt sulfide (O-N-Co₉S₈) oxygen electrocatalyst, which shows excellent activity especially for oxygen evolution reaction (OER), and good stability over 900 charge-discharge cycles at 10 mA cm⁻² in Zinc-air battery. Moreover, we found that O-N-Co₉S₈ was completely converted into Co₃O₄ after OER, showing oxide is actual active phase. Density functional theory calculations reveal the continuous exposure of oxidized surface Co sites during O-N-Co₉S₈ → Co₃O₄ is essential for its high OER activity. These Co sites promote the kinetics for OH* transformation to O* and also ensure fast O₂ desorption. Once Co₃O₄ is generated, the high activity is contributed by its resulting characteristic surfaces. Thus, we propose and demonstrate that oxides *in-situ* generated during OER are more active than the directly calcined oxides. This work advances fundamental insight of metal chalcogenides “catalysts” and guides the design of active OER catalysts.

© 2018 Elsevier Inc. All rights reserved.

1. Introduction

The development of efficient bi-functional electro-catalysts for both oxygen reduction reaction (ORR) and oxygen evolution reaction (OER) is of critical importance for rechargeable Zinc-air batteries. Precious metals such as Pt, Ir, Ru are the best performing catalysts for oxygen electro-catalysis in alkaline [1,2]. However, the scarcity and poor catalytic bi-functionality hinder their application in Zinc-air batteries. The most promising non-precious bi-functional catalysts are derived from carbon-transition metals (e.g. Co, Ni, Fe, Mo, etc.) hybrid materials [3]. The carbon, as a support, ensures the good conductivity of the catalysts, and when doped with N, S or transition metal elements, e.g. Fe, Co, it shows excellent ORR activity [4]. On the other hand, the transition metals, especially their oxides, hydroxides, phosphide, sulfide or nitride can exhibit good OER activities [5–8].

Recently, surface engineering, e.g. NH₃ etching, cation or anion substituting, heteroatom doping, of transition metal chalcogenides and nitrides can effectively improve their activities, especially towards OER [9–12]. Many studies have attributed the enhance-

ment of catalytic activities to synergistic effect or vacancy sites on these engineered transition metal surfaces [13–15]. However, other studies have reported that, during OER, there exist a progressive oxidation of the metal-based materials [16–20], and the oxidized metal surfaces might be responsible for the catalytic activity [21,22]. These reports raised a question that, in the absence of post-OER characterization of the as-prepared catalysts, the explanations on catalytic activity might be inadequate and sometime non-convincing [21]. On the other hand, these reports also imply that considering surface oxidation in the development of metal chalcogenides catalyst might be also beneficial for OER activity.

Based on the above, in the present study, we have engineered an efficient bi-functional catalyst with excellent OER activity that consists of mildly oxidized, N-doped imperfect Co₉S₈ crystals supported on N-doped reduce graphite oxide (O-N-Co₉S₈@N-RGO). The origin of its high OER activity (over-potential of 350 mV at current density of 10 mA cm⁻² under 0.1 M KOH) was investigated by conducting experimental and theoretical research, including detailed experimental characterization of the as-prepared catalysts before and after OER reaction, and Density functional theory (DFT) calculation of the OER kinetics on catalyst surfaces. Note that most of the previous DFT studies on OER have been focusing on the thermodynamics of the reaction through Gibbs free energy-based anal-

* Corresponding author.

E-mail address: zhwchen@uwaterloo.ca (Z. Chen).

¹ These authors contributed equally to this work.

ysis [23–27]. Although successful in predicting catalysts' OER activity, a DFT analysis of OER kinetic would be more suitable for the identification of active catalytic sites: it determines the reaction pathway and associated energetics on surface sites, which is a direct determination of catalyst activity. In addition, although the oxidation O-N-Co₉S₈ crystal during OER is expected, some questions still remain. For example, will high OER activity be maintained (good stability performance) after catalysts oxidation, and why? Addressing these questions will provide an in-depth knowledge on the intrinsic OER activity and “stability” of metal chalcogenides and will potentially guide the design of efficient OER catalysts.

2. Experimental section

2.1. Preparation of O-N-Co₉S₈@N-RGO composite

Reduce graphene oxide (RGO) is obtained by thermal-shock heat treating graphene oxide (GO) in Ar at 900 °C for 1 min, in which the GO was synthesized from graphite powder using modified Hummers method [28,29]. Then, 30 mg of RGO was dispersed in 150 mL of water by ultrasonication for 1 h. Cobalt nitrate hexahydrate [Co(NO₃)₂·6H₂O, 655 mg] and sodium dodecyl sulfate [SDS, 865 mg] were added to the RGO dispersion. Ammonia solution (28–30%, 10 mL) was drop-wisely added to the solution with a rate of 5 mL min⁻¹ under stirring at room temperature. The above suspension was then put into oil bath at 90 °C with stirring for 6 h under ambient atmosphere. After that, the solution was naturally cooled down to room temperature. The suspended black product was collected by centrifugation and washed with DDI water and ethanol, and then freeze-dried. The as-obtained powder product, referred to as Co-S-O-N-RGO precursor, was thermal-shock treated under NH₃ atmosphere at 700 °C in tube furnace for 5 mins, and then cooled down to room temperature in Ar. The resulting product is O-N-Co₉S₈@N-RGO composite.

2.2. Characterization

X-ray diffraction (XRD) was carried out on a Rigaku D/Max 2550 X-ray diffractometer with Ni-filtered Cu K α radiation ($\lambda = 1.5418 \text{ \AA}$). The morphology of the as-prepared composite was investigated using field emission scanning electron microscopy (FE-SEM) (Zeiss Ultra Plus, United Kingdom), and high-resolution transmission electron microscopy (HRTEM) instrument (FEI/Philips CM 300, United States). X-ray photoelectron spectroscopy (XPS) (Thermo Scientific K-Alpha XPS spectrometer) was used to investigate the chemical composition of the as-prepared composites. Note that, the post-OER characterizations (e.g. XRD, XPS) were performed using the catalysts sprayed on carbon paper. Thus, their XRD figures show some patterns of the carbon background.

2.3. Electrochemical activity evaluation

The half-cell electrochemical evaluation of the ORR-OER activity of the as-prepared composites were conducted via rotating disk electrode (RDE) voltammetry using a three-electrode system and potentiostat (CH Instruments 760D). Ink solution was prepared by mixing the composites and carbon black (Vulcan Carbon XC-72) in a 2:1 mass ratio in 1-propanol solution with a total mass concentration of 4 mg mL⁻¹. The working electrode was prepared by coating the ink onto a polished glassy carbon disk electrode with an active material loading of 0.40 mg cm⁻². A graphite rod and saturated calomel electrode (SCE) were used as the counter and reference electrodes, respectively. All potentials were referenced to a reversible hydrogen electrode (RHE) by adding a value

of $(0.245 + 0.059 \times \text{pH}) \text{ V}$. The electrolyte is 0.1 M KOH. Cyclic voltammetry (CV) analysis was performed at the scan rate of 50 mV s⁻¹. The ORR and OER activities were measured in the O₂ and N₂ saturated electrolyte, respectively, through LSV at the scan rate of 10 mV s⁻¹. The OER and ORR activity of as-developed catalysts and commercial Pt/C or Ir/C catalysts were normalized by the geometry area of RDE electrode. The potentials in OER and ORR were corrected for iR losses and background current, respectively. The latter is the current obtained when N₂ is purged into the electrolyte in ORR test.

2.4. Rechargeable Zinc-air battery test

The full-cell Zinc-air battery tests were performed using homemade plastic prototypes. Polished Zinc-plate was used as the Zinc electrode. The O-N-Co₉S₈@N-RGO air electrode was prepared by spraying catalyst ink onto the front side of a carbon paper gas diffusion layer (GDL; SGL Carbon 39 BC; Ion Power Inc.) with an active catalyst loading of 0.67 mg cm⁻². The catalyst ink is prepared from 2.67 mg O-N-Co₉S₈@N-RGO composite, 1.33 mg Vulcan XC-72 carbon black, 13.33 mg 15 wt% Nafion (LIQUion solution, Ion Power Inc.) and 5.0 mL 1-propanol. Stainless steel meshes was used as the current collector for the air cathode, in which it was placed in contact with the backside of the carbon paper. The current collector for the Zinc anode is copper foil. The electrolyte is a solution of 6 M KOH and 0.2 M Zn(CH₃COO)₂.

3. DFT calculations

The periodic DFT calculations were performed using the VASP package [30,31]. The Perdew-Burke-Ernzerhof (PBE) functional was used for the exchange and correlation energy terms [32]. A Dudarev “+U” term acting on the Co 3d states (referred as GGA + U) was applied. The U value was set to 2 eV [33,34]. A plane-wave cutoff of 400 eV was used. Using the calculated lattice constant (9.73 Å) for cubic Co₉S₈, (2 × 1) and (1 × 1) supercell were constructed for Co₉S₈ (1 1 1) and (3 1 1) surfaces, respectively. The Co₉S₈ (1 1 1) slab have six atomic layers and there are seven atomic layers in the Co₉S₈ (3 1 1) slab. The lattice parameters of cubic Co₃O₄ is calculated to be 8.05 Å. The Co₃O₄ (1 1 1) and (4 0 0) surface are represented by a 2 × 1 unit cell, whereas the Co₃O₄ (3 1 1) and (4 2 2) surface are modeled by 1 × 1 unit cell. All the slabs have a vacuum height of 15 Å. The O-N-Co₉S₈ (1 1 1) and O-N-Co₉S₈ (3 1 1) surfaces were developed by tuning (removing and substituting) the corresponding Co₉S₈ (1 1 1) and (3 1 1) slabs, respectively, into the same Co, S, O, N compositions as those observed from XPS analysis (Table S2). Under the specific composition, local stable slab configurations were determined by optimizing extensive slabs with different O, N and S distributions. When the resulting local stable O-N-Co₉S₈ (1 1 1) and O-N-Co₉S₈ (3 1 1) slabs were used to study the OER kinetics, the bottom three atomic layers were fixed, whereas the remaining layers and the adsorbates were allowed to relax. Same atom constrain setting was applied to the Co₉S₈ (1 1 1), (3 1 1) and Co₃O₄ slabs. The k-space was sampled using a 2 × 2 × 1 Monkhorst–Pack grid. Structures are fully relaxed until the forces acting on the atoms are smaller than 0.03 eV/Å. The reaction transition states are determined using the climbing image nudged elastic band method (CI-NEB) [35] and confirmed by vibration analysis with only one negative frequency.

4. Results and discussion

The O-N-Co₉S₈@N-RGO composite was developed by “thermal shock” heat treatment of the Co, S, N and RGO-containing precursor

sor (Co-S-O-N-RGO) under NH_3 atmosphere at 700°C for 5 min. The merits of such synthesis procedure are: (i) the thermal shock heat treatment can result in a fast and imperfect Co_9S_8 crystallization process; (ii) NH_3 as a reduction agent not only prevents the formation of cobalt oxides during calcination, but also provides the N doping source for N-RGO and Co_9S_8 during crystallization. The formation of N-RGO (Fig. S1) is aiming to improve the ORR activity of the composite, which makes it a bifunctional catalyst for Zinc-air battery. For Co_9S_8 crystallization, the NH_3 treatment would result in S-deficient Co_9S_8 surfaces with distorted bulk crystal structure; (iii) using RGO rather than GO as precursor component ensures a mild oxidation of the Co_9S_8 crystal surfaces when NH_3 atmosphere was changed to Ar right after the thermal shock treatment. A highly oxidized catalyst surface might form calcined cobalt oxides. As discussed later, a mild oxidized and imperfect Co_9S_8 crystal rather than calcined cobalt oxides is more beneficial for OER. These features of the O-N- Co_9S_8 @N-RGO composite are confirmed by characterization analyses.

Fig. 1a, and 1b show the SEM and HRTEM images of the O-N- Co_9S_8 @N-RGO composite, respectively. The two lattice fringes with d-spacing of 0.29 and 0.49 nm in HRTEM indicates that (3 1 1) and (1 1 1) planes of Co_9S_8 are the exposed catalyst surfaces. Hereafter, these two surfaces are referred to as O-N- Co_9S_8 (3 1 1) and O-N- Co_9S_8 (1 1 1). Additional HRTEM images are provided in Fig. S2, showing the O-N- Co_9S_8 particle is dominated with (3 1 1) surface. TEM-EDS mapping of the O-N- Co_9S_8 @N-RGO composite clearly indicates the N-insertion in the bulk Co_9S_8 crystal (Fig. 1c), in which Co, S and N are uniformly distributed within the particle. The O element, however, was found on both the RGO sheet and the outer surface of O-N- Co_9S_8 particle, suggesting surface oxidation of the Co_9S_8 crystal. The formation of distorted cubic Co_9S_8 crystal was confirmed by XRD characterization (Fig. 1d). As compared with the standard pattern of cubic Co_9S_8 , the characteristic peaks of O-N- Co_9S_8 @N-RGO was slightly shifted to higher angle, especially for the peak around 52° , suggesting a small shrinkage of the Co_9S_8 crystal. This shrinkage might have been caused by the smaller atomic radius of doped N (65 pm) than S (88 pm). A profile fitting of the O-N- Co_9S_8 peaks with standard cubic Co_9S_8 (lattice parameter: $a = 9.927 \text{ \AA}$) gives a residual error of 6.69%. The calculated lattice parameter of O-N- Co_9S_8 is found to be $a = 9.825 \text{ \AA}$, verifying the shrinkage of its cubic structure. In the Co 2p XPS spectra of O-N- Co_9S_8 @N-RGO composite (before OER), there is a sharp Co $2p_{3/2}$ peak around 778.3 eV (Fig. 1e). This peak is very close to that of metallic Co (777.9 eV), suggesting the reduced nature of Co on the Co_9S_8 surface [36–38]. In the S 2p spectrum (Fig. 1f, before OER), the peaks at 161.4 eV and 162.5 eV agree with the $2p_{3/2}$ and $2p_{1/2}$ state in Co-S bonding. The minor O-Co peak (530.1 eV) in O1s spectrum (Fig. 1g, before OER) indicates that its surface is only slightly oxidized.

The activity of O-N- Co_9S_8 @N-RGO was measured by linear sweep voltammetry (LSV) with 0.1 M KOH solution. The results show that it delivers an ORR onset potential of 0.91 V, and a half-wave potential of 0.81 V (Fig. 1g). Although the ORR performance of the as-prepared composite still cannot provide the same performance as that obtained with the Pt/C catalyst, it exhibits a much lower OER over-potential ($\sim 350 \text{ mV}$) than commercial Ir/C (20%Ir supported on Vulcan XC-72, $\sim 392 \text{ mV}$) when a current density of 10 mA cm^{-2} is generated (Fig. 1i). This indicates that this composite is one of the best performing OER catalysts in mild alkaline media (Table S1). In addition to the O-N- Co_9S_8 @N-RGO, O-N- Co_9S_8 and N-RGO were synthesized to distinguish the active ORR and OER component in the composite (Fig. 1h and i). The synthesis procedures are presented in the Supporting Information. The results show that: (i) O-N- Co_9S_8 and N-RGO alone only have limited ORR activity, highlighting the importance of combining Co and N-RGO in improving ORR performance; (ii) although the

N-RGO can further enhance the OER activity, the OER activity of the O-N- Co_9S_8 @N-RGO is mainly contributed by the O-N- Co_9S_8 phase. Fig. 1i shows that the activity the O-N- Co_9S_8 @N-RGO was maintained after 2000 cyclic voltammetry cycles (from 0.9 to 1.7 V vs. RHE). Moreover, the current–time curve with the applied potentials at 1.60 V vs. RHE shows that the O-N- Co_9S_8 @N-RGO electrode delivers a stable current over 20 h of continuous operation (Fig. 2a), implying its good “stability” for OER. When used as air electrode (catalyst loading of 0.67 mg cm^{-2}) in Zinc-air battery, O-N- Co_9S_8 @N-RGO demonstrates comparable and even better charge performance with that of Pt/C + Ir/C particularly at high current densities (Fig. 2b). In addition, a long-term cyclability for over 200 h (at 10 mA cm^{-2}) was achieved in ambient air (Fig. 2c), indicating that the O-N- Co_9S_8 @N-RGO composite exhibits excellent cycling performance for OER.

The morphology and composition of the O-N- Co_9S_8 @N-RGO catalyst after OER half-cell test (at constant potential of 1.60 V vs. RHE) were examined. The XRD pattern (Fig. 1d) and HRTEM images (Fig. 1j) showed that, after 9 h of OER reaction, O-N- Co_9S_8 crystals were converted to aggregated Co_3O_4 particles (Fig. S3). This suggests that there is a phase transformation during OER, which might also be facilitated by the doped and imperfect crystallization nature of O-N- Co_9S_8 . The interplanar spacings on Co_3O_4 are 0.16, 0.20 and 0.24 nm, respectively, which corresponds to the d-spacing (4 2 2), (4 0 0) and (3 1 1) lattice planes of cubic Co_3O_4 . This is consistent with that shown in FFT pattern (inset Fig. 1j). TEM-EDS mapping of the sample after OER reveals that most of S was replaced by O, whereas N was no longer observed in the mapping analysis (Fig. 1k). This observation suggests that N (or at least most of N) was removed after OER, which is also supported by the N1s XPS analysis (Fig. S1). The Co 2p XPS spectra of the post-OER (after 4 and 9 h reaction) O-N- Co_9S_8 @N-RGO catalyst is identical to that obtained from com- Co_3O_4 . By integrating the peak area of Co^{3+} and Co^{2+} , the $\text{Co}^{3+}/\text{Co}^{2+}$ ratio was found to be 1.93:1, which is in very close agreement with the theoretical value of $\text{Co}^{3+}/\text{Co}^{2+} = 2:1$ in Co_3O_4 ; this result further supports the transformation of O-N- Co_9S_8 to Co_3O_4 . The very minor Co-S peak after OER reaction, as shown in S2p XPS spectrum (Fig. 1f), also confirms the replacement of S by O in O-N- Co_9S_8 particle. The increased intensity of SO_4^{2-} peaks imply that most of the residue S exists in the form of SO_4^{2-} . The substitution of S by O is also supported by the increased intensity of O-Co peak in O1s XPS spectrum (Fig. 1g, after OER).

The above analyses confirmed the complete oxidation of O-N- Co_9S_8 into Co_3O_4 during OER. As shown in previous half-cell and Zinc-air durability test (Fig. 2a, and c), even after 9 h, the catalyst still exhibits excellent OER performance, e.g. in half-cell RDE durability test, the output current dropped by 15% after 20 h. That is, the high OER activity was maintained during, and even after the transformation of O-N- Co_9S_8 to Co_3O_4 . This raises another question: how is this achieved? Interestingly, we found that the (1 1 1) lattice plane of Co_3O_4 , featured with large interplanar spacing (0.46 nm), was not detected in the present HRTEM imaging analysis. It is one of the typical surfaces that is commonly observed in calcined Co_3O_4 (Fig. S3c). Therefore, based on the above observations, it is reasonable to assume that: (i) the OER active site is surface Co; (ii) the status of surface Co sites was maintained during the transition of O-N- Co_9S_8 into Co_3O_4 under OER; (iii) the Co sites in the resulting Co_3O_4 (3 1 1), (4 2 2), (4 0 0) surfaces are more active or stable for OER than its (1 1 1) plane, and therefore should be responsible for the high OER activity of the post-OER (or *in-situ* generated) Co_3O_4 phase. Note that previous studies have reported the formation of $\text{Co}(\text{OH})_2$ and CoOOH species during OER on CoO_x catalysts in XPS and *in-situ* surface-enhanced Raman spectroscopy analysis [39–41]. This is very likely to occur during OER, especially

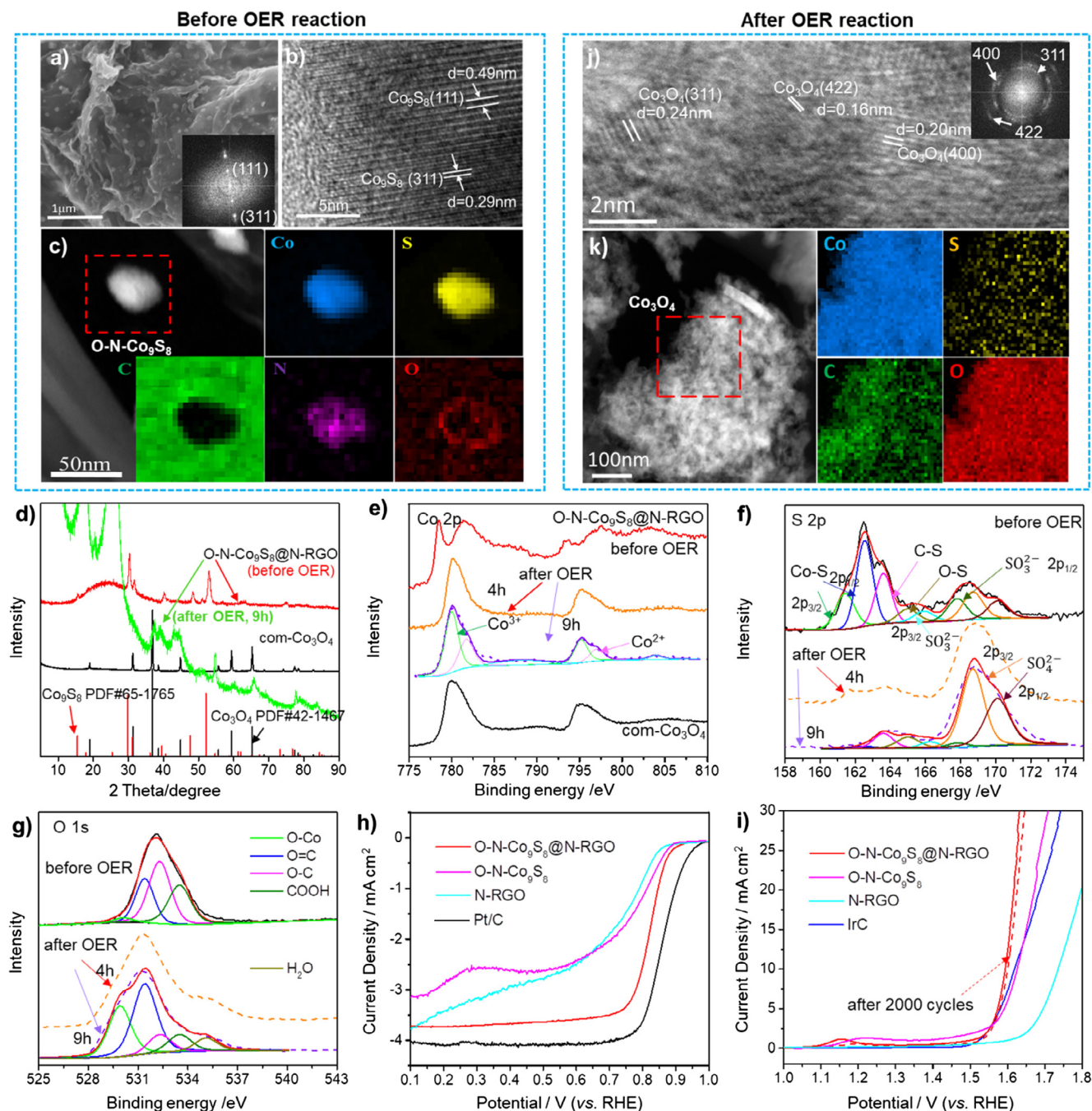


Fig. 1. (a) SEM; (b) HRTEM images, and (c) TEM-EELS mapping images of O-N-Co₉S₈@N-RGO before OER reaction; (d) XRD patterns; (e) XPS spectra of the Co 2p; (f) S 2p; (g) O 1s in O-N-Co₉S₈@N-RGO before and after OER reaction; (h) ORR activities evaluated by RDE LSV at rotating speed of 900 r.p.m.; (i) OER activities at RDE (1600 r.p.m) in 0.1 M KOH electrolyte. LSV is adopted at a scan rate of 10 mV s⁻¹; (j) HRTEM and (k) TEM-EELS mapping images of O-N-Co₉S₈@N-RGO after 9 h OER half-cell test at constant potential of 1.60 V vs. RHE.

on the out-most Co₉S₈/Co₃O₄ surfaces that are in close contact with the OH⁻ reactant. In fact, as it will be shown with our DFT analysis, the OER reaction actually occurs between the OH-Co-OH and OH-Co-O intermediate surface configurations (Fig. 3, Fig. S4). Bulk-Pourbaix thermodynamics have indicated that, as the potential increases, the stability of Co states increases as Co(OH)₂ < Co₃O₄ < CoOOH < CoO₂, and Co²⁺ is predicted unstable at the OER region (above 1.23 V vs RHE) [42,43]. Interestingly, in the present study, there is no evidence for the formation of Co(OH)₂, CoOOH and CoO₂ species even in the XPS analysis. One possible explanation might be the formation of CoOOH (Co³⁺) and CoO₂ (Co⁴⁺) from Co₉S₈ is kinetically unfavorable at 1.65 V vs RHE, because of the less

oxidative S in the composite. These S could stabilize the low oxidation state Co²⁺. Meanwhile, the replacement of S and with O would consume many OH⁻ lowering the local concentration of OH⁻ on the catalyst surface. As a result, the oxidation kinetics for Co²⁺ to Co³⁺ or Co⁴⁺ might be hindered. Moreover, considering the fact that: (i) the formation of Co(OH)₂ and CoOOH bulk crystals have been rarely reported; (ii) in the present study, Co₃O₄ crystal was indeed produced during OER, this indicates that Co₃O₄ is the real stable phase formed in OER when Co₉S₈ is used as the “catalyst”.

To verify this assumption and have a deeper understanding on the origins of enhanced activity and “stability” of cobalt sulfide “catalyst”, the OER elementary reaction kinetics on O-N-Co₉S₈

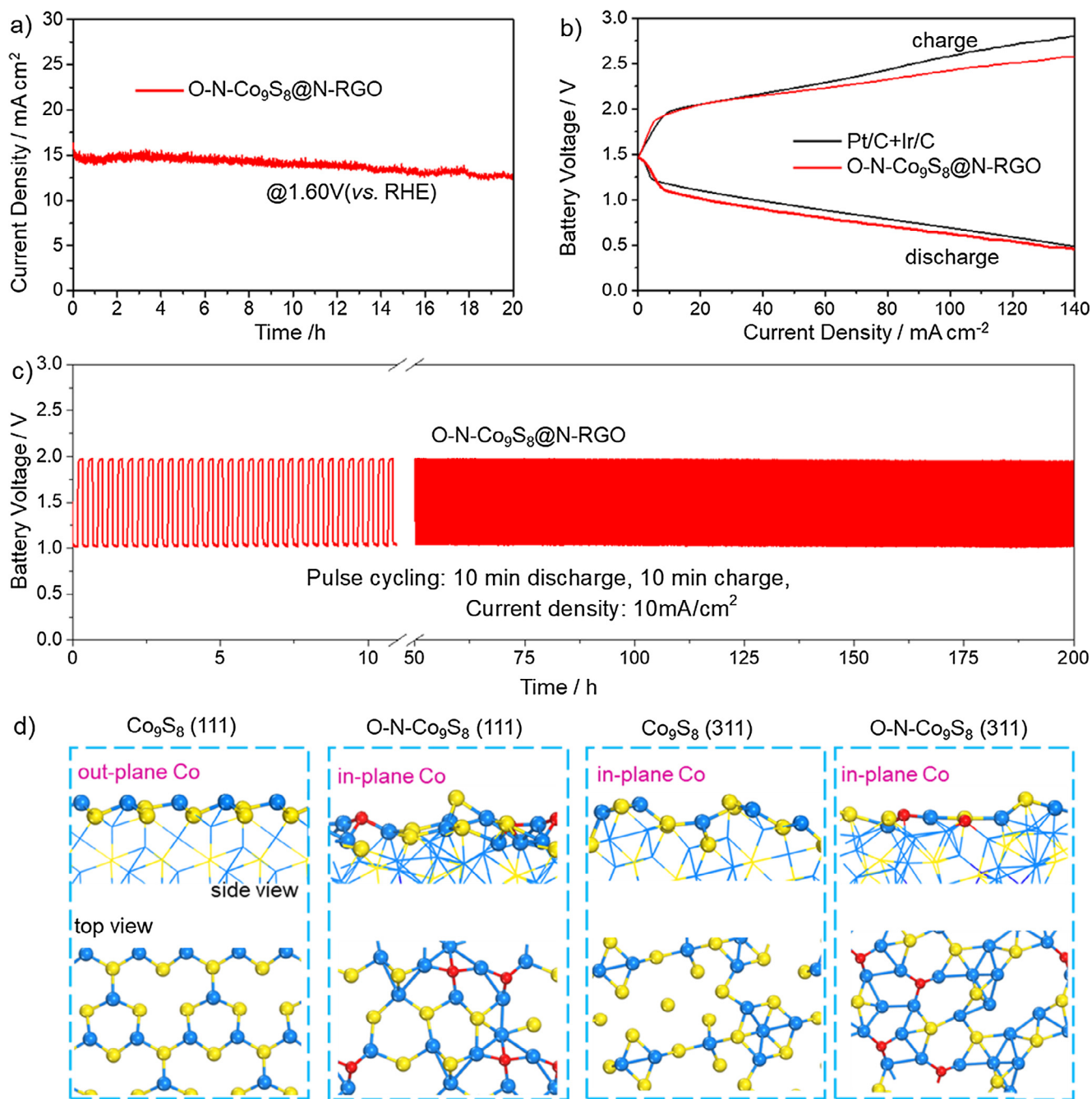


Fig. 2. (a) Long-term OER electrolysis stability of O-N-Co₉S₈@N-RGO under constant potential; (b) Charge and discharge polarization curves, and (c) Cycling performance of Zinc-air battery assembled using O-N-Co₉S₈@N-RGO as air electrode in ambient air; (d) Slab models of the ideal Co₉S₈ and O-N-Co₉S₈ (1 1 1) and (3 1 1) surfaces. Only the outmost atomic layer was shown. Blue: Co; Red: O; Yellow: S. Note that N was not shown here, because it was found more stable in the inner sublayers than on the outmost surface layer.

and Co₃O₄ were investigated by DFT within the GGA + U framework (see DFT calculations section). Noted that, although our experiments have demonstrated that O-N-Co₉S₈ is not stable and will be oxidized into Co₃O₄, O-N-Co₉S₈ has been considered in the DFT calculations to evaluate its OER activity at the initial reaction stage. This can provide a better comparison on the origin of OER activity before and after O-N-Co₉S₈ oxidation. The DFT models for the O-N-Co₉S₈ catalyst were developed based on the surface composition evaluated from XPS analysis and its exposed surfaces, e.g. (1 1 1) and (3 1 1), observed in HRTEM (Fig. 1b). Thus, two slab models, referred to as O-N-Co₉S₈ (1 1 1) and O-N-Co₉S₈ (3 1 1),

were used to represent the O-N-Co₉S₈ catalyst. Fig. 2d shows the local stable slab configurations of the two models, which were chosen among extensive optimized slabs with different O, N and S distributions under the XPS-evaluated composition. Details on the estimation of the surface composition can be found in the Supplementary Information 3. In addition to the O-N-Co₉S₈ (1 1 1) and O-N-Co₉S₈ (3 1 1) models, two other models featuring ideal Co₉S₈ (1 1 1) and Co₉S₈ (3 1 1) surfaces were also considered (Fig. 2d). The *in-situ* generated Co₃O₄ catalyst was modeled by Co₃O₄ (3 1 1), Co₃O₄ (4 2 2) and Co₃O₄ (4 0 0) surfaces, as observed in the HRTEM image (Fig. 1j). The Co₃O₄ (1 1 1) surface was also

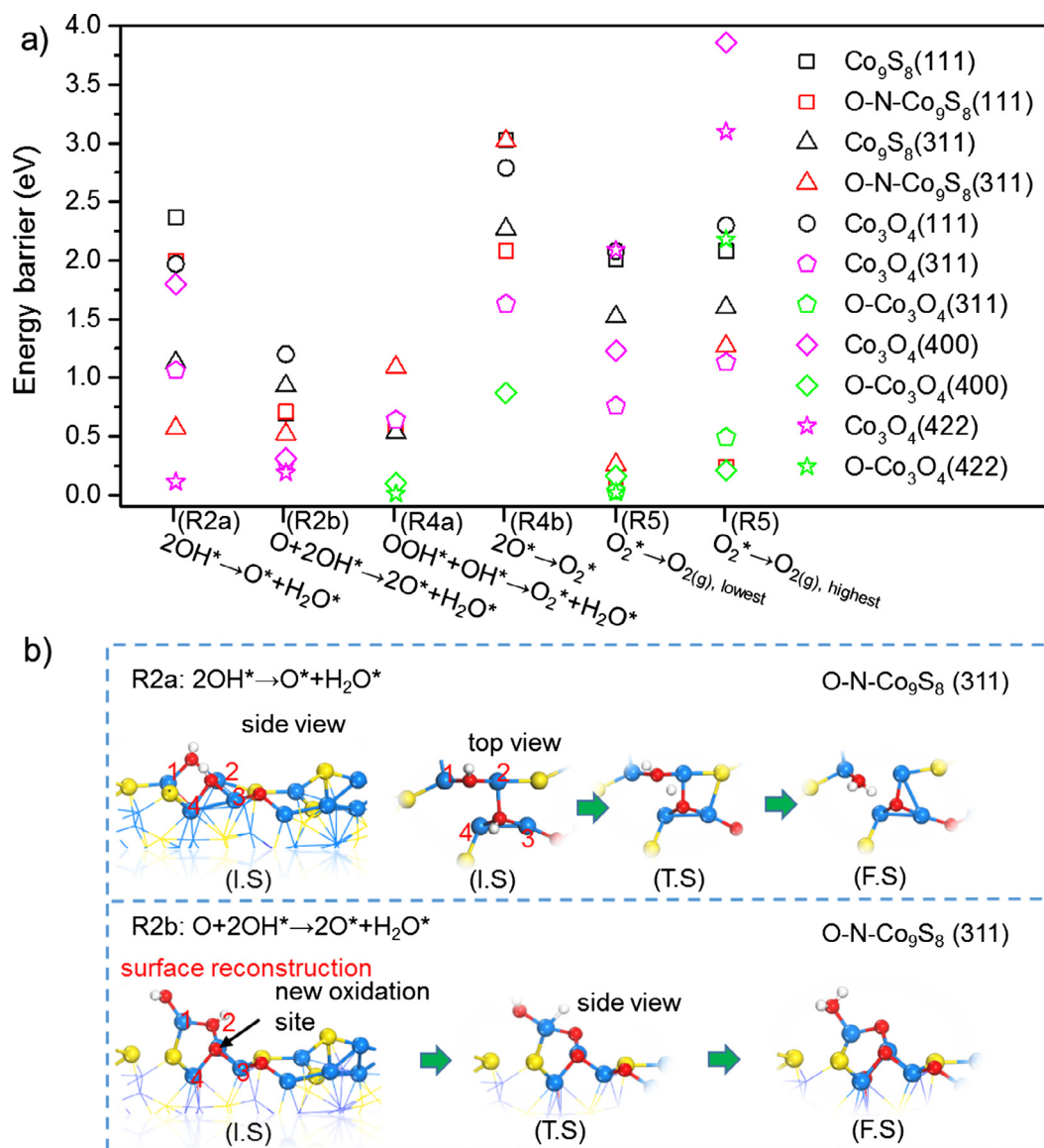
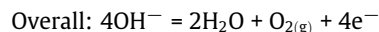
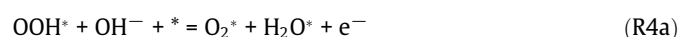
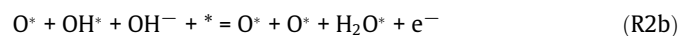
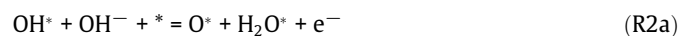


Fig. 3. (a) Energy barriers for the OER elementary steps on different catalyst surfaces, and (b) reaction pathways along the transformation of OH^{*} to O^{*} on O-N-Co₉S₈ (3 1 1) surface. Blue: Co; Red: O; Yellow: S; White: H. I.S: initial state; T.S: transition state; F.S: final state.

considered for the sake of comparison. The comparison of the OER kinetics between these catalyst surface models will provide a comprehensive understanding on the OER activity of Co₉S₈ and Co₃O₄ based catalysts.

In this study, the following widely accepted OER reaction mechanism was considered [44]:



Herein, there are a few points that need to be clarified: (i) R1 is a potential-dependent reaction, and it can be considered as non-activated OH⁻ surface adsorption and e⁻ release process. Thus, activation energy was not required; (ii) the activation barriers for R2-R4a are potential and coverage dependent. Also, strictly speaking, the cell-size extrapolated explicitly solvated NEB-type barrier calculations should be performed to consider the solvent effect. However, this would make the study very complex. For the present study, our objective is to give an initial evaluation on the OER activity of O-N-Co₉S₈ and Co₃O₄ surfaces, and therefore the energy barriers for R2-R4a were approximated from the energy barriers of their analogous chemical (non-electrochemical) reactions by assuming that the transition state (T.S.) of an analogous chemical reaction represents the T.S. for the electrochemical reaction [45–49]. Since the electrode potential changes the energy of OH⁻; the applied positive potential will only further lower the OER energy barrier estimated from the analogous chemical reactions in DFT. Thus, the analogous chemical reaction barriers

obtained from DFT represents the initial or reference energy barriers, and can be used to evaluate the intrinsic activity of the catalysts towards R2-R4a without applying potential. Therefore, in order to simplify the calculations, the DFT analysis was performed on the basis of the realistic models for O-N-Co₉S₈ and Co₃O₄ materials in the absence of applied potential and solvent effect; (iii) R2a and R2b are similar, but R2b considers the effect of local surface oxidation (nearby site occupied by O^{*}); (iv) in R3, the formation of OOH^{*} is assumed to be produced from direct attachment of OH⁻ from the electrolyte solution with surface O^{*}. DFT calculations show that its analogous chemical reaction is a very favorable process. That is, as long as the OH⁻ is not a surface species (OH^{*}), the geometry optimization of such system will always result into the formation of OOH^{*}. Accordingly, R3 is assumed as fast reaction and no energy barriers need to be overcome; v) R4b and R5 are chemical (non-electrochemical) reactions, which are independent of potential. One may argue that O^{*}, as the reactant, its surface coverage is potential-dependent, and therefore both R4b and R5 are related to potential. Here, the effect of O^{*} coverage (or potential) on the two reactions will be limited. This is because, based on the high OER activity of the as-developed catalyst, O^{*} coverage cannot be not very high. Otherwise, it will totally block the active Co sites and hinders R1 reaction and the reactions involving H₂O formation (R2a, R2b and R4a) as well; (vi) in R5, the adsorption energy of O₂ can be considered as the energy barrier of the production of gas phase O₂(g). The adsorption energy of O₂ is defined as a positive value. Accordingly, a higher value means O₂ adsorption is

strong, which would limit its desorption kinetics. Therefore, the present study focuses on the energetics for OH^{*} to O^{*} transformation (R2a and R2b), OOH^{*} to O₂^{*} transformation (R4a), O₂^{*} formation from O^{*} and its desorption to O₂(g).

The activation barriers for the elementary steps R2-R5 are presented in Fig. 3a. The observations found on the cobalt sulfide catalysts (O-N-Co₉S₈ and ideal Co₉S₈) are as follows: (i) reaction R2b always proceed with lower energy barriers (0.52–0.93 eV) than R2a (0.57–2.31 eV), suggesting local surface oxidation promotes the transformation of OH^{*} to O^{*}. Such effect is profound on ideal Co₉S₈ (1 1 1) surface, which can be attributed to the destabilization effect of the local oxidation on OH^{*} adsorption: the local oxidation (O^{*}) will push away its adjacent OH^{*} from the stable Co bridge site (Fig. S4), and therefore destabilize it, making it more reactive with its neighboring OH^{*}. This also explains the low energy barrier (0.57 eV) of R2a observed on O-N-Co₉S₈ (3 1 1), which occurs next to a pre-existing oxidation (O) site (Fig. 3b). Interestingly, after the creation of a new oxidation site (reaction R2b in Fig. 3b), surface reconstruction on the O-N-Co₉S₈ (3 1 1) was observed: the oxidized Co atom was pushed outwards, breaking the existing Co-S lattice and exposing it to the incoming OH⁻. It forms a configuration that one OH^{*} occupies the outward exposed Co atom, the other OH^{*} sits beside it on the Co bridge site. The OH^{*} transformation to O^{*} was promoted by such reconstructed Co sites associated with a low energy barrier (0.52 eV). The enhancement of OH^{*} to O^{*} transformation by neighboring O sites was also reported by Rossmeisl and coworkers [24], and their explanation for this phenomenon

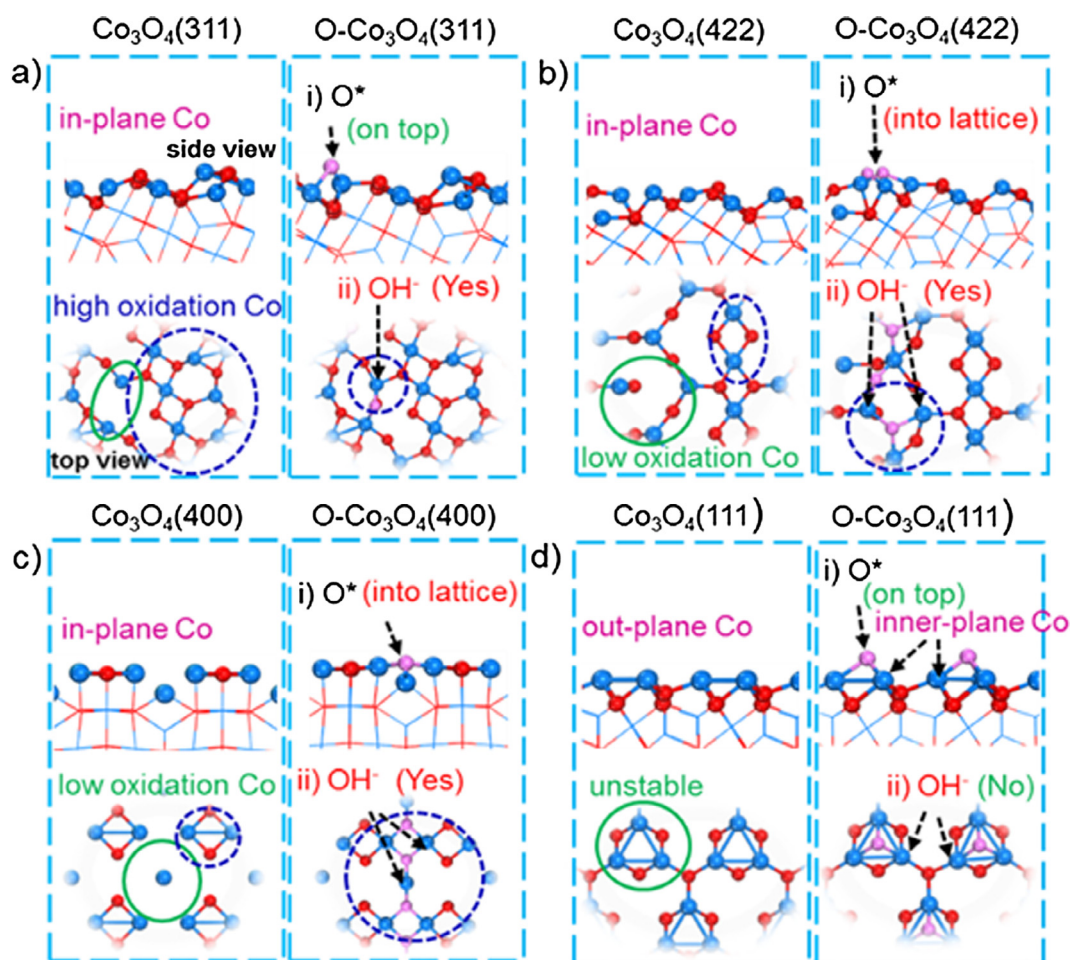


Fig. 4. Surface topology of the ideal Co₃O₄ surfaces and their corresponding oxidized surfaces. Only the outmost atomic layer was shown. Blue: Co; Red: O; Magenta: oxidation O.

is that the bridging O could adsorb the H in *OH , and therefore favors the direct dissociation of OH^* into O^* ; (ii) OOH^* can only have a stable form on catalyst surfaces that have high oxidation state in-plane Co site, in which the Co is coordinated with O or S atoms (at least two) in the same plane of the outmost surface layer. The O-N- Co_9S_8 and ideal Co_9S_8 surfaces have the in-plane Co sites, expect ideal Co_9S_8 (1 1 1), see Fig. 2d. On ideal Co_9S_8 (1 1 1) surface, the Co are located on top of the outmost S atoms. Such out-plane Co sites act as strong “hosts” for O^* and OH^* adsorption, making OOH^* automatically dissociates into O^* and OH^* during structure optimization and further hinders O_2^* production. However, on O-N- Co_9S_8 (1 1 1) surface, stable OOH^* was observed, and OOH^* transformation to O_2 is very fast (energy barrier of 0.57 eV).

Therefore, the transformation of OOH^* to O_2^* (R4a) is more likely to occur on stabilized in-plane Co sites, and the formation of such in-plane Co sites can be realized by the oxidation reaction during the phase transition of surface-engineered O-N- Co_9S_8 to Co_3O_4 under OER; (iii) The high activation energies associated with reaction R4b (≥ 2.08 eV) suggest that O_2^* production from two neighboring O^* is very unlikely to occur on both O-N- Co_9S_8 and Co_9S_8 models. That is, O_2 is produced from OOH^* ; (iv) Fig. 3a presents the lowest and highest O_2^* adsorption energy obtained at different sites on each surface model. The adsorption energy of O_2^* on the ideal Co_9S_8 surfaces were found to be very high (1.52–2.08 eV). However, on the O-N- Co_9S_8 (1 1 1) and (3 1 1) surfaces, desorption O_2^* is significantly enhanced, i.e. the barriers drop to 0.15–1.27 eV

suggesting that oxidized surfaces may promote the OER kinetics by quickly releasing surface O_2^* to the gas phase $O_{2(g)}$.

On the *in-situ* generated ideal Co_3O_4 catalyst models, similar results were obtained: (i) when compared to that in R2a, the transformation of OH^* to O^* is promoted by the local oxidation site (R2b) on all the ideal Co_3O_4 surfaces, and its activity follows: (4 2 2) > (3 1 1) > (4 0 0) > (1 1 1) with energy barriers of 0.19, 0.29, 0.31, and 1.20 eV, respectively (Fig. 3a); (ii) the Co_3O_4 (3 1 1) surface is mainly composed of a high oxidation state in-plane Co sites (Fig. 4a). The Co on (4 2 2) and (4 0 0) surfaces also located on in-plane sites, but some of them are in low oxidation state (Fig. 4b and c). Same as the ideal Co_9S_8 (1 1 1) surface, the Co_3O_4 (1 1 1) surface contains only out-plane Co sites (Fig. 4d). Therefore, OOH^* was found to be stable on ideal (3 1 1) surface, and its transformation to O_2^* is fast with a low energy barrier of 0.64 eV; (iii) O_2^* production from two neighboring O^* is kinetically unfavorable, especially on the out-plane Co sites on ideal Co_3O_4 (1 1 1); (iv) among the ideal Co_3O_4 models, O_2^* desorption is most favorable on the ideal (3 1 1) surface, because of its high oxidation state Co sites.

By far, the ideal Co_3O_4 (3 1 1) surface is the only plane that is favorable for OER reaction. However, in realistic conditions, the low oxidation state and out-plane Co sites on the ideal Co_3O_4 surfaces might be oxidized (occupied by O^*) during OER reaction. Therefore, the oxidized Co_3O_4 surfaces, referred to as O- Co_3O_4 (3 1 1), O- Co_3O_4 (4 2 2), O- Co_3O_4 (4 0 0) and O- Co_3O_4 (1 1 1) were considered. Since most of the Co sites on ideal (3 1 1) surface are

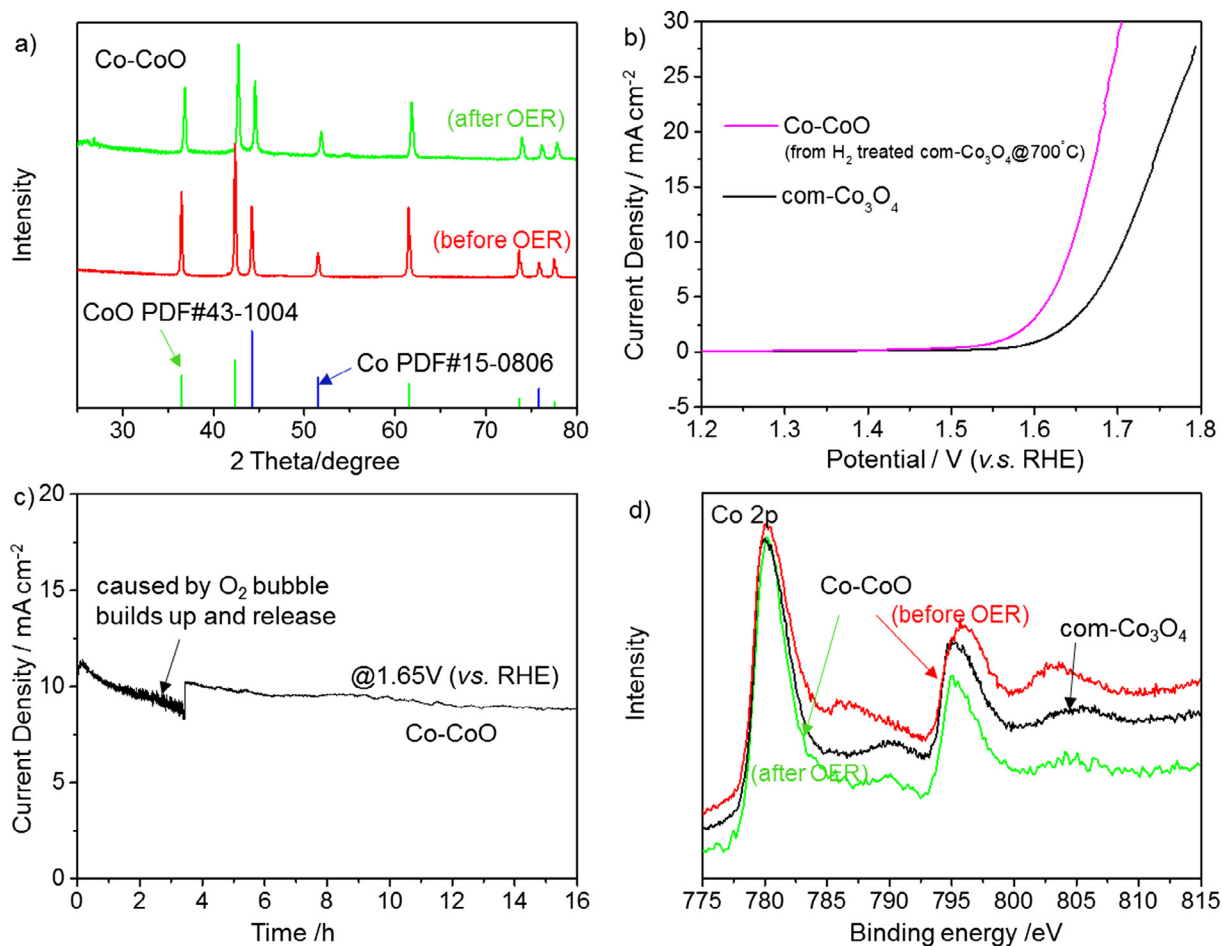


Fig. 5. (a) XRD and (b) OER activities of Co-CoO (obtained from H₂ treatment of com-Co₃O₄) at RDE (1600 r.p.m) in 0.1 M KOH electrolyte at LSV scan rate of 10 mV s⁻¹; (c) Long-term electrolysis stability of Co-CoO composite under constant potential in RDE test; (d) Co 2p XPS spectra of the Co-CoO composite before and after 9 h OER test at constant potential of 1.65 V (vs. RHE).

in high oxidation state, the occupation of O^* on top of a few local low oxidation state Co sites should not affect its activity, as illustrated in Fig. 4a. However, on the O-Co₃O₄ (4 2 2) and O-Co₃O₄ (4 0 0), the oxidation occurs within the in-plane Co lattice: O^* was incorporated into the outmost surface layer (Fig. 4b and c), and therefore oxidizing the low oxidation state in-plane Co into high oxidation state. As discussed above, such in-plane Co sites are favorable for OOH[•] transformation to O₂[•] (R4a), and O₂[•] desorption (R5) as well. This was verified by the energetic analysis for R4a and R5 on O-Co₃O₄ (4 2 2) and O-Co₃O₄ (4 0 0) surfaces (Fig. 3a). Note that, although stable OOH[•] was observed, once it is placed next to OH[•], they will be transformed into O₂[•] and H₂O[•] during geometry optimization. Therefore, no transition state for R4a was found on O-Co₃O₄ (4 2 2) and O-Co₃O₄ (4 0 0) surfaces. The low energy barriers labeled for these two surfaces in Fig. 3a were used to illustrate that the transformation of OOH[•] to O₂[•] is automatic from the DFT analysis. For the ideal Co₃O₄ (1 1 1) surface, once it was oxidized into O-Co₃O₄ (1 1 1), it forms an oxidation layer with O^* sites on the out-most atomic surface (Fig. 4d). It blocks the Co sites, and prevents its interaction with the incoming OH⁻ reactant.

In addition to the kinetic calculations, a thermodynamic analysis of the Co₈S₉/Co₃O₄ surfaces toward the OH[•] → O^* reaction (R2a and R2b) was performed (Table S1). This reaction is selected because it is the most possible potential limiting step as revealed by its relative high energy barrier among the elementary reactions (Fig. 3a). The reaction free energy and overpotential of the OH[•] → O^* reaction show that the thermodynamic evaluation on the activity of Co₈S₉/Co₃O₄ surfaces toward the reaction is consistent with that predicted by the kinetic analysis, including: (i) the existence of neighboring O^* lowers the overpotential for OH[•] → O^* reaction, especially for the (3 1 1) surfaces in Co₉S₈; (ii) the activity of ideal Co₃O₄ surfaces predicted by thermodynamic analysis is also consistent with that predicted by kinetic analysis: (4 2 2) > (3 1 1) > (4 0 0) > (1 1 1); (iii) the oxidized Co₃O₄ surfaces is more favorable for OH[•] → O^* transformation than ideal surfaces. Details on the calculation method can be found in the Supporting Information.

Based on the above, our results indicate that, regardless of Co oxidation state, Co₃O₄ (1 1 1) surface is not favorable for OER, and the high OER activity of the *in-situ* generated Co₃O₄ was contributed by its oxidized, characteristic high-index surface planes, e.g. (3 1 1), (4 2 2) and (4 0 0). This is consistent with the experimental study by Wei et al. [50], in which they reported that the exposed Co₃O₄ (1 1 2) high-index facet shows much lower overpotential for OER than (1 1 1) surface. This might explain the higher OER activity of this *in-situ* generated Co₃O₄ than many reported calcined Co₃O₄ catalysts (Table S1). The latter usually contains exposed Co₃O₄ (1 1 1) plane (Fig. S3c). This means that, although Co₃O₄ has been confirmed as the real stable OER catalytic phase, the direct synthesis of Co₃O₄ by calcination might not be a suitable approach for preparing efficient OER catalyst. The Co₃O₄ obtained from phase transition under OER might be more active than calcined Co₃O₄ crystals. To further support this argument, we reduced the com-Co₃O₄ in H₂ (10%)/Ar atmosphere at 700 °C for 5mins. The XRD and XPS Co2p spectrum show the resulting product is a composite of Co-CoO crystals, and the surface Co is in the state of CoO (Fig. 5). As expected, in RDE test, it exhibits a ~50 mV lower overpotential (at 10 mA cm⁻²) for OER than com-Co₃O₄ (Fig. 5b). As shown in Fig. 5c, the Co-CoO composite delivers a stable OER performance under continuous operation at an applied potential of 1.65 V vs. RHE. Post-OER characterizations show that, after 9 h OER test at 1.65 V vs. RHE, the Co-CoO crystals remained intact (Fig. 5a). However, the state of surface Co was transformed from CoO into Co₃O₄ (Fig. 5d). Similar results were also obtained for our calcined hollow Co₃O₄ catalyst: when reduced by H₂, the resulting hollow CoO-Co₃O₄ composite shows a ~35 mV lower OER overpotential than the original hollow Co₃O₄ particle (Fig. S5).

5. Conclusions

A O-N-Co₉S₈@N-RGO composite was designed as an efficient and stable bifunctional catalyst for Zinc-air batteries. It was developed on the basis of imperfect crystallization and surface engineering, e.g. oxidation and nitrogen doping, of Co₉S₈ crystals to achieve a high catalytic activity in particularly for OER. When used as the air electrode catalyst, the Zinc-air battery exhibits significantly reduced discharge and charge overpotentials and outstanding long cycling stability over 200 cycles at 10 mA cm⁻². Moreover, post-characterizations reveal that O-N-Co₉S₈ was completely converted into Co₃O₄ after OER, confirming Co₃O₄ is the real stable catalytic phase. As there are increasingly many reports claiming transition metal sulfides as highly efficient OER catalysts, this observation further clarifies what the OER catalyst really is. Moreover, our DFT analysis reveals that the exposed oxidized surface Co sites could significantly lower the reaction barriers of key reaction steps in OER, suggesting that such Co sites are the active sites on O-N-Co₉S₈ and Co₃O₄. Therefore, we concluded that the continuous exposure of these oxidized Co sites during O-N-Co₉S₈ transition into Co₃O₄ is essential for the cycling performance of such catalyst. This is made possible by (i) the surface reconstruction during O-N-Co₉S₈ transition into Co₃O₄; and (ii) the unique Co sites topology on the exposed planes of *in-situ* generated Co₃O₄. With such knowledge, our study suggests, and experimentally shows that, *in-situ* generated metal oxides, e.g. Co₃O₄, from phase transition of metal chalcogenides, or reduced metal oxides during OER, should be more active than the calcined oxides crystals. This work advances the fundamental insights on the activity and “stability” of metal chalcogenides-based OER “catalysts”, providing guidance for the design of active OER catalysts.

Acknowledgments

The authors would like to acknowledge the financial support from the Natural Sciences and Engineering Research Council of Canada. This work was made possible by access to the facilities of the Shared Hierarchical Academic Research Computing Network and Compute/Calcul Canada.

Appendix A. Supplementary material

Supplementary data associated with this article can be found, in the online version, at <https://doi.org/10.1016/j.jcat.2018.08.020>.

References

- [1] B. Lim, M. Jiang, P.H.C. Camargo, E.C. Cho, J. Tao, X. Lu, Y. Zhu, Y. Xia, *Science* 324 (2009) 1302.
- [2] T. Reier, M. Oezaslan, P. Strasser, *ACS Catal.* 2 (2012) 1765.
- [3] B. Hua, M. Li, Y.-F. Sun, Y.-Q. Zhang, N. Yan, J. Chen, T. Thundat, J. Li, J.-L. Luo, *Nano Energy* 32 (2017) 247.
- [4] G. Wu, A. Santandreu, W. Kellogg, S. Gupta, O. Ogoke, H. Zhang, H.-L. Wang, L. Dai, *Nano Energy* 29 (2016) 83.
- [5] Q. Wang, L. Shang, R. Shi, X. Zhang, G.I.N. Waterhouse, L.-Z. Wu, C.-H. Tung, T. Zhang, *Nano Energy* 40 (2017) 382.
- [6] H. Zhu, J. Zhang, R. Yanzhang, M. Du, Q. Wang, G. Gao, J. Wu, G. Wu, M. Zhang, B. Liu, J. Yao, X. Zhang, *Adv. Mater.* 27 (2015) 4752.
- [7] S. Dou, L. Tao, J. Huo, S. Wang, L. Dai, *Energy Environ. Sci.* 9 (2016) 1320.
- [8] T. Zhou, Y. Du, D. Wang, S. Yin, W. Tu, Z. Chen, A. Borgna, R. Xu, *ACS Catal.* 7 (2017) 6000.
- [9] M. Chauhan, K.P. Reddy, C.S. Gopinath, S. Deka, *ACS Catal.* 7 (2017) 5871.
- [10] P. Ganesan, M. Prabu, J. Sanetuntikul, S. Shanmugam, *ACS Catal.* 5 (2015) 3625.
- [11] J. Wang, W. Cui, Q. Liu, Z. Xing, A.M. Asiri, X. Sun, *Adv. Mater.* 28 (2016) 215.
- [12] G.-F. Chen, T.Y. Ma, Z.-Q. Liu, N. Li, Y.-Z. Su, K. Davey, S.-Z. Qiao, *Adv. Funct. Mater.* 26 (2016) 3314.
- [13] C. Tang, H.-S. Wang, H.-F. Wang, Q. Zhang, G.-L. Tian, J.-Q. Nie, F. Wei, *Adv. Mater.* 27 (2015) 4516.
- [14] J. Fu, F.M. Hassan, C. Zhong, J. Lu, H. Liu, A. Yu, Z. Chen, *Adv. Mater.* 29 (2017) 1702526.

- [15] L. Zhuang, L. Ge, Y. Yang, M. Li, Y. Jia, X. Yao, Z. Zhu, *Adv. Mater.* 29 (2017) 1606793.
- [16] M.E.G. Lyons, M.P. Brandon, *J. Electroanal. Chem.* 641 (2010) 119.
- [17] C. Spçri, H.J.T. Kwan, Ar. Bonakdarpour, D.P. Wilkinson, P. Strasser, *Angew. Chem. Int. Ed.* 56 (2017) 5994.
- [18] X. Xu, F. Song, X. Hu, *Nat. Commun.* 7 (2016) 12324.
- [19] C. Yang, O. Fontaine, J.-M. Tarascon, A. Grimaud, *Angew. Chem. Int. Ed.* 56 (2017) 8652.
- [20] B. Song, K. Li, Y. Yin, T. Wu, L. Dang, M. Cabán-Acevedo, J. Han, T. Gao, X. Wang, Z. Zhang, J.R. Schmidt, P. Xu, S. Jin, *ACS Catal.* 7 (2017) 8549.
- [21] S. Jin, *ACS Energy Lett.* 2 (2017) 1937.
- [22] Y. Zhang, B. Ouyang, J. Xu, G. Jia, S. Chen, R.S. Rawat, H.J. Fan, *Angew. Chem. Int. Ed.* 55 (2016) 8670.
- [23] I.C. Man, H.Y. Su, F. Calle-Vallejo, H.A. Hansen, J.I. Martínez, N.G. Inoglu, J. Kitchin, T.F. Jaramillo, J.K. Nørskov, *J. Rossmeisl, ChemCatChem* 3 (2011) 1159.
- [24] N.B. Halck, V. Petrykin, P. Krtil, J. Rossmeisl, *Phys. Chem. Chem. Phys.* 16 (2014) 13682.
- [25] B.J. Kim, D.F. Abbott, X. Cheng, E. Fabbri, M. Nachtegaal, F. Bozza, I.E. Castelli, D. Lebedev, R. Schaublin, C. Copéret, T. Graule, N. Marzari, T.J. Schmidt, *ACS Catal.* 7 (2017) 3245.
- [26] T. Qiu, B. Tu, D. Saldana-Greco, A.M. Rappe, *ACS Catal.* 8 (2018) 2218.
- [27] M. Garcia-Mota, M. Bajdich, V. Viswanathan, A. Vojvodic, A.T. Bell, J.K. Nørskov, *J. Phys. Chem. C* 116 (2012) 21077.
- [28] W.S. Hummers Jr, R.E. Offeman, *J. Am. Chem. Soc.* 80 (1958) 1339.
- [29] Y. Xu, H. Bai, G. Lu, C. Li, G. Shi, *J. Am. Chem. Soc.* 130 (2008) 5856.
- [30] G. Kresse, J. Hafner, *J. Phys. Rev. B.* 47 (1993) 558.
- [31] G. Kresse, J. Furthmüller, *J. Phys. Rev. B.* 54 (1996) 11169.
- [32] J.P. Perdew, K. Burke, M. Ernzerhof, *Phys. Rev. Lett.* 77 (1996) 3865.
- [33] L. Wang, T. Maxisch, G. Ceder, *Phys. Rev. B* 73 (2006) 195107.
- [34] X.Y. Pang, C. Liu, D.C. Li, C.Q. Lv, G.C. Wang, *ChemPhysChem* 14 (2013) 204.
- [35] G. Henkelman, B.P. Uberuaga, H. Jonsson, *J. Chem. Phys.* 113 (2000) 9901.
- [36] L.H. Jin, C.C. Lv, J. Wang, H. Xia, Y.X. Zhao, Z.P. Huang, *Am. J. Analyt. Chem.* 7 (2016) 210.
- [37] J. Wang, L. Li, X. Chen, Y. Lu, W. Yang, *J. Mater. Chem. A* 4 (2016) 11342.
- [38] F. Morales, F.M.F. de Groot, O.L.J. Gijzeman, A. Mens, O. Stephan, B.M. Weckhuysen, *J. Catal.* 230 (2005) 301.
- [39] N. Weidler, S. Paulus, J. Schuch, J. Klett, S. Hoch, P. Stenner, A. Maljusch, J. Brötz, C. Wittich, B. Kaisera, W. Jaegermann, *Phys. Chem. Chem. Phys.* 18 (2016) 10708.
- [40] B.S. Yeo, A.T. Bell, *J. Am. Chem. Soc.* 133 (2011) 5587.
- [41] K.S. Exner, J. Anton, T. Jacob, H. Overa, *Electrochim. Acta* 120 (2014) 460.
- [42] J. Chivot, L. Mendoza, C. Mansour, T. Pauporte, M. Cassir, *Corrosion Sci.* 50 (2008) 62.
- [43] M. Bajdich, M. García-Mota, A. Vojvodic, J.K. Nørskov, A.T. Bell, *J. Am. Chem. Soc.* 135 (2013) 13521.
- [44] J. Rossmeisl, Z.W. Qu, H. Zhu, G.J. Kroes, J.K. Nørskov, *J. Electroanal. Chem.* 607 (2007) 83.
- [45] H.J. Chun, V. Apaja, A. Clayborne, K. Honkala, J. Greeley, *ACS Catal.* 7 (2017) 3869.
- [46] X. Nie, M.R. Esopi, M.J. Janik, A. Asthagiri, *Angew. Chem. Int. Ed.* 52 (2013) 2459.
- [47] J. Wang, K. Li, H. Zhong, D. Xu, Z. Wang, Z. Jiang, Z. Wu, X. Zhang, *Angew. Chem. Int. Ed.* 54 (2015) 10530.
- [48] M.R. Singh, J.D. Goodpaster, A.Z. Weber, M. Head-Gordon, A.T. Bell, *PNAS* 114 (2017) 8812.
- [49] E. Skúlason, V. Tripkovic, M.E. Björketun, S. Gudmundsdóttir, G. Karlberg, J. Rossmeisl, T. Bligaard, H. Jónsson, J.K. Nørskov, *J. Phys. Chem. C* 114 (2010) 18182.
- [50] R. Wei, M. Fang, G. Dong, C. Lan, L. Shu, H. Zhang, X. Bu, J.C. Ho, *A.C.S. Appl. Mater. Interfaces* 10 (2018) 7079.